














CrossMark

# The Massive and Distant Clusters of *WISE* Survey. VI. Stellar Mass Fractions of a Sample of High-redshift Infrared-selected Clusters

Bandon Decker<sup>1</sup>, Mark Brodwin<sup>1</sup> , Zubair Abdulla<sup>2,3</sup> , Anthony H. Gonzalez<sup>4</sup> , Daniel P. Marrone<sup>5</sup> , Christine O'Donnell<sup>5</sup>, S. A. Stanford<sup>6</sup>, Dominika Wylezalek<sup>7</sup> , John E. Carlstrom<sup>2,3</sup>, Peter R. M. Eisenhardt<sup>8</sup>, Adam Mantz<sup>9,10</sup>, Wenli Mo<sup>4</sup> , Emily Moravec<sup>4</sup> , Daniel Stern<sup>8</sup> , Greg Aldering<sup>11</sup>, Matthew L. N. Ashby<sup>12</sup> , Kyle Boone<sup>11,13</sup> , Brian Hayden<sup>11,14</sup> , Nikhel Gupta<sup>15</sup>, and Michael A. McDonald<sup>16</sup>

<sup>1</sup> Department of Physics and Astronomy, University of Missouri, 5110 Rockhill Road, Kansas City, MO 64110, USA

<sup>2</sup> Kavli Institute for Cosmological Physics, University of Chicago, 5640 South Ellis Avenue, Chicago, IL 60637, USA

<sup>3</sup> Department of Astronomy and Astrophysics, University of Chicago, 5640 South Ellis Avenue, Chicago, IL 60637, USA

<sup>4</sup> Department of Astronomy, University of Florida, 211 Bryant Space Center, Gainesville, FL 32611, USA

<sup>5</sup> Steward Observatory, University of Arizona, 933 North Cherry Avenue, Tucson, AZ 85721, USA

<sup>6</sup> Department of Physics, University of California, One Shields Avenue, Davis, CA 95616, USA

<sup>7</sup> European Southern Observatory, Karl Schwarzschild Straße 2, D-85748, Garching bei München, Germany

<sup>8</sup> Jet Propulsion Laboratory, California Institute of Technology, Pasadena, CA 91109, USA

<sup>9</sup> Kavli Institute for Particle Astrophysics and Cosmology, Stanford University, 382 Via Pueblo Mall, Stanford, CA 94305-4060, USA

<sup>10</sup> Department of Physics, Stanford University, 382 Via Pueblo Mall, Stanford, CA 94305-4060, USA

<sup>11</sup> Lawrence Berkeley National Laboratory, 1 Cyclotron Road, MS 50B-4206, Berkeley, CA 94720, USA

<sup>12</sup> Harvard-Smithsonian Center for Astrophysics, 60 Garden Street, Cambridge, MA 02138, USA

<sup>13</sup> Department of Physics, University of California, 366 LeConte Hall MC 7300, Berkeley, CA 94720, USA

<sup>14</sup> Space Telescope Science Institute, 3700 San Martin Drive, Baltimore, MD 21218, USA

<sup>15</sup> School of Physics, University of Melbourne, Grattan Street, Parkville, VIC 3010, Australia

<sup>16</sup> Kavli Institute for Astrophysics and Space Research, Massachusetts Institute of Technology, 77 Massachusetts Avenue, Cambridge, MA 02139, USA

Received 2018 November 29; revised 2019 March 18; accepted 2019 March 22; published 2019 June 14

## Abstract

We present measurements of the stellar mass fractions ( $f_*$ ) for a sample of high-redshift ( $0.93 \leq z \leq 1.32$ ) infrared-selected galaxy clusters from the Massive and Distant Clusters of *WISE* Survey (MaDCoWS) and compare them to the stellar mass fractions of Sunyaev–Zel’dovich (SZ) effect-selected clusters in a similar mass and redshift range from the South Pole Telescope (SPT)–SZ Survey. We do not find a significant difference in mean  $f_*$  between the two selection methods; though, we do find an unexpectedly large range in  $f_*$  for the SZ-selected clusters. In addition, we measure the luminosity function of the MaDCoWS clusters and find  $m^* = 19.41 \pm 0.07$ , similar to other studies of clusters at or near our redshift range. Finally, we present SZ detections and masses for seven MaDCoWS clusters and new spectroscopic redshifts for five MaDCoWS clusters. One of these new clusters, MOO J1521+0452 at  $z = 1.31$ , is the most distant MaDCoWS cluster confirmed to date.

*Key words:* cosmology: observations – galaxies: clusters: general – galaxies: clusters: intracluster medium

## 1. Introduction

Galaxy clusters are the largest gravitationally bound objects in the universe and a thorough knowledge of their composition, history, and evolution is important for both cosmological abundance analyses and galaxy formation/evolution studies in the richest environments (e.g., Allen et al. 2011; Kravtsov & Borgani 2012). It has been found in simulations (e.g., Ettori et al. 2006; Conroy et al. 2007) and suggested observationally (e.g., Lin et al. 2003) that the fraction of a cluster’s total mass that is in stars,  $f_*$ , is related to the star formation history of that cluster. It follows that measuring  $f_*$  and  $f_{\text{gas}}$ , the fraction of mass in the intracluster medium (ICM), in clusters covering a range of masses and ages can constrain the growth and evolutionary history of clusters and the galaxies therein. A proper account of the total stellar mass of a cluster is also a necessary component of calculating the total baryon fraction in a cluster. The cluster baryon fraction is expected to be close to the total baryon fraction of the universe (White et al. 1993), but previous studies (e.g., Gonzalez et al. 2007, 2013; Lin et al. 2012) have found somewhat lower fractions. The size of this discrepancy and its relation to the total mass of the cluster is important cosmologically and can also provide clues to the baryon physics in clusters (He et al. 2005). Coupled with

studies that show a cessation of star formation in the cores of large clusters since high redshifts (e.g., Brodwin et al. 2013), such measurements can shed light on the feedback processes involved in the partition of baryons into stars and gas in clusters.

Several studies have previously looked at the stellar mass fraction of clusters and generally find a trend of decreasing  $f_*$  with increasing halo mass. However, with the exception of van der Burg et al. (2014), all these studies were at  $z \leq 0.6$  (Lin et al. 2003, 2012; Gonzalez et al. 2007, 2013; Andreon 2010; Zhang et al. 2011) and/or used samples that selected clusters entirely on the strength of the signal from the ICM, either from X-ray observations or from the Sunyaev–Zel’dovich (SZ, Sunyaev & Zeldovich 1970, 1972) decrement (Giodini et al. 2009; Hilton et al. 2013; Chiu et al. 2016, 2018). It is possible, for both SZ- and X-ray-selected samples, that selecting an observable related to the ICM pressure or X-ray luminosity (approximately ICM density squared) could produce a sample with a bias toward a higher gas mass fraction, presumably at the expense of  $f_*$  (assuming a constant baryon fraction at fixed mass). Such a bias may also prevent the scatter in  $f_{\text{gas}}$  from being fairly measured, though the measured scatter in  $f_*$  should be less affected, as the cluster selection does not have any intrinsic bias toward or against stellar mass.

To explore these issues, we use high-redshift infrared-selected clusters from the Massive and Distant Clusters of WISE Survey (MaDCoWS, Gettings et al. 2012; Stanford et al. 2014; Brodwin et al. 2015; Gonzalez et al. 2015, 2018; Mo et al. 2018). MaDCoWS uses the *Wide-field Infrared Survey Explorer* (Wright et al. 2010) AllWISE data release (Cutri 2013) and PanSTARRS (Chambers et al. 2016) optical data to identify overdensities of galaxies at  $z \sim 1$  across nearly the entire extragalactic sky. It therefore can provide a greater mass range at high-redshift than SZ surveys because it simultaneously has the area to find the rarest, most massive objects at high redshifts—such as MOO J1142+1527 ( $M_{500} = 5.36 \times 10^{14} M_{\odot}$ ,  $z = 1.19$ ) reported in Gonzalez et al. (2015) and MOO J1521+0452 ( $M_{500} = 3.59 \times 10^{14} M_{\odot}$ ,  $z = 1.31$ ) described herein—and the sensitivity to detect clusters to the same or lower mass limit than current SZ surveys.

In this work we use SZ observations and follow-up *Spitzer Space Telescope* data on 12 MaDCoWS clusters to calculate  $f_*$  for this high-redshift, infrared-selected sample. We also analyze a comparable sample of 33 SZ-selected clusters from the South Pole Telescope (SPT)–SZ survey (Bleem et al. 2015) using the same methodology and compare these to the same quantities measured for our infrared-selected MaDCoWS clusters. Because the SPT sample is SZ-selected, it fairly measures the average value and scatter in  $f_*$ .

The cluster samples and data we use are described in Section 2 and the analysis thereof is described in Section 3. We present the results of our  $f_*$  measurements in Section 4 and discuss them in Section 5. Our conclusions are in Section 6. Throughout we use AB magnitudes and a concordance  $\Lambda$ CDM cosmology of  $\Omega_m = 0.3$ ,  $\Omega_{\Lambda} = 0.7$  and  $H_0 = 70 \text{ km s}^{-1} \text{ Mpc}^{-1}$ . We define  $r_{500}$  as the radius inside which a cluster has an average density 500 times the critical density of the universe and  $M_{500}$  as the mass inside that radius.

## 2. Cluster Sample and Data

For our infrared-selected sample, we use 12 MaDCoWS clusters with halo masses calculated from SZ detections from the Combined Array for Research in Millimeter-wave Astronomy (CARMA). SZ observations of four of these (MOO J0319-0025, MOO J1014+0038, MOO J1155+3901, and MOO J1514+1346) are described in Brodwin et al. (2015). A fifth, MOO J1142+1527, the most massive cluster yet found by any method at  $z \geq 1.15$ , is reported in Gonzalez et al. (2015). Here we report new SZ detections for the other seven clusters, along with total masses and radii determined from those data as well as new masses and radii of the previously reported clusters derived from an updated reduction of the CARMA data, described in Section 3.1. All 12 clusters have imaging with the Infrared Array Camera (IRAC; Fazio et al. 2004) on *Spitzer*, which enables us to determine the stellar mass of the clusters as described in Section 4.1.

The SZ-selected clusters we use for comparison are drawn from the SPT–SZ survey described in Bleem et al. (2015). To ensure we are making a fair comparison between the infrared- and SZ-selected samples, we only use the 33 SPT clusters that lie in a similar range of mass and redshift as the MaDCoWS clusters, specifically  $0.9 < z < 1.35$  and  $M_{500} < 1 \times 10^{15} M_{\odot}$ , and for which comparable IRAC data exist. We do not impose a lower limit on the mass for the SPT subsample as the SPT–SZ catalog has a higher mass threshold than MaDCoWS at these

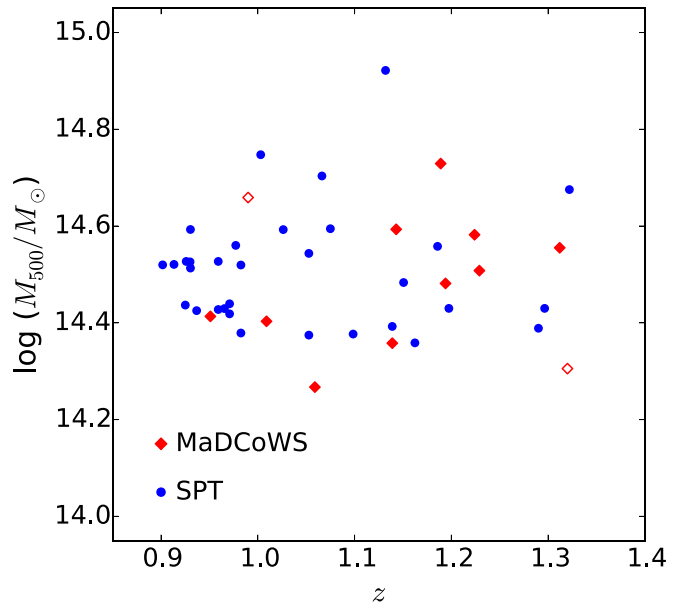


**Figure 1.** Plot showing the distribution of the MaDCoWS clusters (red diamonds) and the comparison SPT clusters (blue circles) in mass and redshift. The open diamonds denote the MaDCoWS clusters in this analysis that currently lack spectroscopic redshifts.

redshifts. A plot of mass versus redshift for both samples is shown in Figure 1.

### 2.1. CARMA Data

Before its closure in early 2015, CARMA was a heterogeneous 23-element interferometer with six 10.4 m antennae, nine 6.1 m antennae, and eight 3.5 m antennae. All of the antennae were equipped with 30 and 90 GHz receivers and the 10.4 and 6.1 m antennae had additional 230 GHz receivers. CARMA had two correlators, a wide-band and spectral-line correlator, and the 3.5 m antennae could operate as an independent array (CARMA-8 mode) or alongside the other 15 antennae in CARMA-23 mode. In its most compact ‘E’ configuration, the shortest CARMA baselines provided an appropriate beam size for SZ observations while the longer baselines enabled point-source identification and subtraction.

The CARMA data for the seven new clusters were taken in the summer and fall of 2014 and the observation dates of all 12 of our MaDCoWS clusters, as well as the on-source observation times excluding observations of the gain and flux calibrators, are given in Table 1. Point-source-subtracted SZ maps of the seven clusters newly reported here are shown in Figure 2. The maps are in units of signal-to-noise with negative signal to denote the SZ effect being a decrement at 30 GHz. A  $4k\lambda$  taper was applied to the  $uv$  data to produce an illustrative beam size and the maps were CLEANed (Högbom 1974) in a box  $4'$  on a side and centered on the SZ centroid.

### 2.2. Spitzer Data

Eight of the MaDCoWS clusters were observed in *Spitzer* Cycle 9 (Program ID 90177; PI Gonzalez) and have  $6 \times 30$  s depth in the IRAC 3.6  $\mu\text{m}$  and 4.5  $\mu\text{m}$  channels, while the remaining four were observed to the same depth as part of a Cycle 11–12 snapshot program (PID 11080; PI Gonzalez). This depth allows us to detect objects down to one magnitude fainter than the characteristic magnitude ( $m^*$ ) on all of our clusters

**Table 1**  
Summary of CARMA Observations and Properties of MaDCoWS Clusters

Cluster ID	R.A. (J2000)	Decl. (J2000)	UT Dates	Exp. Time <sup>a</sup> (hr)	S/N ( $\sigma$ )	$z$	$Y_{500}$ ( $10^{-5} M_{\odot}$ )	$r_{500}$ (Mpc)	$M_{500}$ ( $10^{14} M_{\odot}$ )
MOO J0037+3306	00:37:45.8	+33:06:51	2014 Sep 12,27–28	6.0	3.3	1.139	$1.78^{+0.87}_{-0.73}$	$0.62^{+0.05}_{-0.06}$	$2.26^{+0.62}_{-0.61}$
MOO J0105+1323 <sup>e</sup>	01:05:31.5	+13:23:55	2014 Jul 6; Oct 11	7.3	8.1	1.143	$1.49^{+0.91}_{-0.80}$	$0.72 \pm 0.03$	$3.92^{+0.46}_{-0.44}$
MOO J0123+2545	01:23:50.3	+25:45:31	2014 Sep 27	1.9	4.4	1.229	$4.47^{+1.76}_{-1.43}$	$0.70 \pm 0.05$	$3.86^{+0.85}_{-0.79}$
MOO J0319–0025 <sup>b</sup>	03:19:24.4	–00:25:21	2013 Sep 30	1.0	5.7	1.194	$2.97^{+0.75}_{-0.78}$	$0.65^{+0.03}_{-0.04}$	$2.97^{+0.75}_{-0.78}$
MOO J1014+0038 <sup>b</sup>	10:14:08.4	+00:38:26	2013 Oct 6–7	2.2	8.0	1.230	$3.34^{+0.64}_{-0.52}$	$0.66 \pm 0.02$	$3.22^{+0.36}_{-0.31}$
MOO J1111+1503	11:11:42.6	+15:03:44	2014 Jul 23,25	4.4	5.0	1.32 <sup>d</sup>	$1.58^{+0.41}_{-0.37}$	$0.54 \pm 0.04$	$2.02^{+0.30}_{-0.30}$
MOO J1142+1527 <sup>c</sup>	11:42:45.1	+15:27:05	2014 Jul 3	5.0	10.4	1.189	$7.70^{+1.36}_{-1.17}$	$0.79 \pm 0.03$	$5.36^{+0.55}_{-0.50}$
MOO J1155+3901 <sup>b</sup>	11:55:45.6	+39:01:15	2012 May 11–12	7.2	2.9	1.009	$2.05^{+0.72}_{-0.65}$	$0.66^{+0.04}_{-0.05}$	$2.53^{+0.50}_{-0.51}$
MOO J1231+6533	12:31:14.8	+65:33:29	2014 Sep 7–8	1.5	4.3	0.99 <sup>d</sup>	$5.76^{+2.83}_{-1.80}$	$0.81^{+0.07}_{-0.06}$	$4.69^{+1.27}_{-1.24}$
MOO J1514+1346 <sup>b,e</sup>	15:14:42.7	+13:46:31	2013 Jun 1,3,5–7,9,11	8.4	2.8	1.059	$1.91^{+0.73}_{-0.97}$	$0.63^{+0.04}_{-0.08}$	$2.39^{+0.51}_{-0.83}$
MOO J1521+0452	15:21:04.6	+04:52:08	2014 Sep 23	2.5	2.7	1.312	$4.13^{+2.14}_{-1.61}$	$0.66 \pm 0.07$	$3.59^{+1.02}_{-0.92}$
MOO J2206+0906 <sup>e</sup>	22:06:28.6	+09:06:32	2014 Jul 5,8	5.7	3.1	0.951	$2.58^{+1.30}_{-0.92}$	$0.71 \pm 0.06$	$2.95^{+0.82}_{-0.68}$

#### Notes.

<sup>a</sup> On-source, unflagged.

<sup>b</sup> Brodwin et al. (2015), with a mass and radius recalculated from an improved CARMA reduction pipeline.

<sup>c</sup> Gonzalez et al. (2015), with a mass and radius recalculated from an improved CARMA reduction pipeline and using a slightly different cosmology.

<sup>d</sup> Photometric redshift estimated from IRAC 3.6  $\mu\text{m}$  and 4.5  $\mu\text{m}$  images, with error  $\sim 0.07$ .

<sup>e</sup> Identified as a merging cluster from follow-up *Chandra* imaging (see Gonzalez et al. 2018).

with high (>70%) completeness. The SPT clusters were observed with *Spitzer* over four Cycles (PID 60099, 70053, 80012, 10101; PI Brodwin) to a depth of  $8 \times 100$  s in 3.6  $\mu\text{m}$  and  $6 \times 30$  s in 4.5  $\mu\text{m}$ .

### 2.3. Optical Data

Five of the MaDCoWS clusters have follow-up  $r$ - and  $z$ -band imaging with the Gemini Multi-Object Spectrograph (GMOS; Hook et al. 2004) on Gemini-North with five 180 s exposures in the  $r$ -band and twelve 80 s exposures in the  $z$ -band from programs GN-2013A-Q-44 and GN-2013B-Q-8 (PI Brodwin). The data were taken between 2013 February and 2015 July.

### 2.4. New Spectroscopic Redshifts

Five of the MaDCoWS clusters presented here have previously unreported spectroscopic redshifts. We obtained spectroscopic observations of these five clusters from 2015 through 2017, primarily with the Low Resolution Imaging Spectrometer (LRIS; Oke et al. 1995) at the W. M. Keck Observatory, the details of which are given in Table 2. The mask used for each cluster was designed from the *Spitzer* imaging and focused on the IRAC sequence members identified in a 3.6–4.5  $\mu\text{m}$  color–magnitude diagram.

One of the clusters with new spectroscopic redshifts reported here, MOO J1521+0452, is the highest-redshift MaDCoWS cluster with spectroscopy, and with  $M_{500} = (3.59^{+1.02}_{-0.92}) \times 10^{14} M_{\odot}$ , it is the third-most massive cluster to be found at  $z \geq 1.3$  by any method. The spectroscopy confirmed six cluster members and established  $z = 1.312$  as the cluster redshift. Representative spectra of two of the confirmed members are shown in Figure 3.

Four cluster members were confirmed for MOO J0037+3306, establishing the cluster redshift of  $z = 1.133$ . MOO J0105+1323 and MOO J0123+2545 each had five identified members, placing their redshifts at  $z = 1.143$  and  $z = 1.215$ , respectively.

In addition to the newly reported clusters above, we also present a new spectroscopic redshift for MOO J1014+0038, previously reported at a photometric redshift of  $z_{\text{phot}} = 1.27 \pm 0.08$  (Brodwin et al. 2015). In addition to LRIS spectroscopy, we also observed this cluster with the Multi-Object Spectrometer For Infra-Red Exploration (McLean et al. 2010, 2012) at Keck on 2016 February 1. These new spectra identified seven members and established the redshift for MOO J1014+0038 as  $z = 1.231$ . Spectra for two of these members are shown in Figure 4.

## 3. Analysis

### 3.1. Total Cluster Mass

Details of the CARMA observations are given in Table 1. The data, including those for clusters previously reported in Brodwin et al. (2015) and Gonzalez et al. (2015), were re-reduced using a new MATLAB pipeline designed specifically for CARMA data. Mars was used as the flux calibrator for each cluster with the Rudy et al. (1987) flux model and observations of a bright monochromatic quasar were interleaved with the cluster observations for gain calibration. The cluster Comptonization ( $Y_{\text{SZ}}$ ) was calculated by using a Monte Carlo Markov Chain to fit an Arnaud et al. (2010) pressure profile and point-source models (where indicated by the long baseline data) to the CARMA data in  $uv$  space. The significance of the detection was calculated by comparing  $\chi^2$  for the fit to the Arnaud model and point source(s) to  $\chi^2$  for a fit to just the point source(s) with no cluster model.  $M_{500}$  and  $r_{500}$  were calculated from  $Y_{\text{SZ}}$  by forcing consistency with the scaling relation from Andersson et al. (2011). The resulting masses, radii, and  $Y_{\text{SZ}}$  values are shown in Table 1. Updated masses and radii, based on the new pipeline, are reported for the clusters reported in Brodwin et al. (2015) and Gonzalez et al. (2015). These are all consistent within  $1\sigma$  with the originally reported quantities. The  $M_{500}$  measurements for the SPT–SZ sample are from the Bleem et al. (2015) catalog.



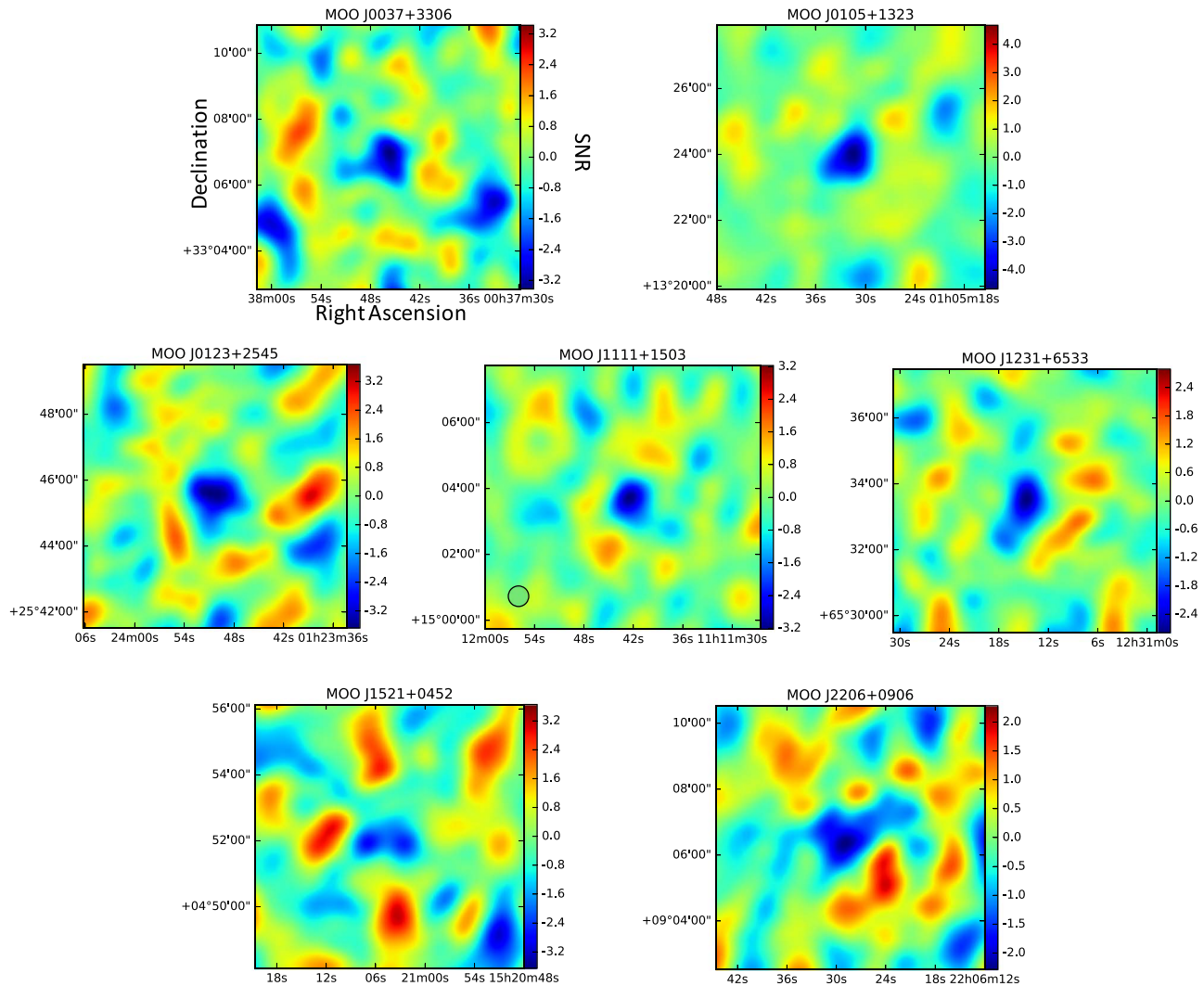


**Figure 2.** CARMA maps of the seven new MaDCoWS clusters presented here. Each map is  $8' \times 8'$ , centered on the centroid of the SZ decrement and in units of signal-to-noise. Emissive point sources have been subtracted out of all the maps and they have all been CLEANed around the decrement. A representative beam pattern is shown in the lower left-hand corner of the map of MOO J1111+1503.

### 3.2. Catalogs

For each cluster we ran SExtractor (Bertin & Arnouts 1996) in dual-image mode on the  $3.6 \mu\text{m}$  and  $4.5 \mu\text{m}$  images, selecting on the  $3.6 \mu\text{m}$  image. We used the IRAC coverage maps as weights and SExtractor parameters similar to those in Lacy et al. (2005). These parameters are optimized for IRAC, but we changed DEBLEND\_NTHRESH to 64 and DEBLEND\_MINCONT to 0.00005 to better deblend sources in the cluster cores. Magnitudes were measured in  $4''$  diameter apertures and corrected to  $24''$  diameter apertures using the corrections from Ashby et al. (2009). Catalogs for the optical images were produced with the same SExtractor parameters, but with MAG\_AUTO magnitudes instead of corrected aperture magnitudes. The optical and infrared catalogs were then matched using the IRAC astrometry to produce combined catalogs for each cluster. All of the catalogs have IRAC 3.6 and  $4.5 \mu\text{m}$  fluxes that are  $\gtrsim 70\%$  complete down to magnitudes of 21.0 and 22.5, respectively. The clusters with optical data have additional  $r$ - and  $z$ -band data similarly complete to depths of 25.5 and 24.5 mag.

### 3.3. Cluster Membership

Because our cluster masses are measured at an overdensity of  $\Delta = 500$ , we only consider galaxies projected within  $r_{500}$  (as determined from the SZ data) from the centroid of the SZ decrement in our measurement of stellar masses and fractions (e.g., Figure 5). To ensure our choice of center does not significantly impact our results, we also ran our analysis using the centroid of the galaxy distribution and using the BCG as the center. We find no appreciable differences in our results. Within  $r_{500}$ , we also reject objects that likely lie in the foreground by not including any source with an apparent magnitude brighter than  $m^* - 2$  at the redshift of our cluster. The effects of this choice of cutoff are discussed in Section 5.4. The characteristic magnitude was calculated using the same model as was used for our K-corrections (described in Section 4.1). To limit the effect of incompleteness at the faint end, we reject objects more than one magnitude fainter than  $m^*$ .

We used the available optical data for five of the MaDCoWS clusters to identify stars in color-color space. Following Eisenhardt et al. (2004), we plot  $r - z$  versus  $z - 3.6 \mu\text{m}$  colors for each of our possible cluster members. To the

**Table 2**  
Spectroscopic Cluster Members

R.A.	Decl.	Instrument	UT Date	$z$	Quality <sup>a</sup>	Features
MOO J0037+3306 $z = 1.133$						
00:37:45.77	+33:07:50.9	LRIS	2016 Aug 5	1.131	A	D4000
00:37:46.18	+33:07:28.2	LRIS	2016 Aug 5	1.123	A	Ca HK
00:37:48.82	+33:07:08.4	LRIS	2016 Aug 5	1.15	B	D4000
00:37:47.03	+33:06:45.7	LRIS	2016 Aug 5	1.13	B	D4000
MOO J0105+1323 $z = 1.143$						
01:05:26.64	+13:23:36.9	LRIS	2015 Dec 4	1.13	B	D4000
01:05:26.20	+13:23:53.7	LRIS	2015 Dec 4	1.14	B	D4000
01:05:29.95	+13:23:54.6	LRIS	2015 Dec 4	1.15	A	Ca HK, D4000
01:05:35.27	+13:23:10.4	LRIS	2015 Dec 4	1.144	B	[O II] $\lambda$ 3727, D4000
MOO J0123+2545 $z = 1.215$						
01:23:50.95	+25:45:47.19	LRIS	2017 Jul 20	1.20	B	D4000
01:23:57.16	+25:44:16.67	LRIS	2017 Jul 20	1.22	B	D4000
01:23:47.37	+25:46:50.65	LRIS	2017 Jul 20	1.2214	A	[O II] $\lambda$ 3727
01:23:41.53	+25:47:32.78	LRIS	2017 Jul 20	1.2196	B	[O II] $\lambda$ 3727
MOO J1014+0038 $z = 1.231$						
10:14:07.31	+00:38:27.1	LRIS	2015 Feb 21	1.231	B	Ca HK
10:14:10.51	+00:37:56.2	LRIS	2015 Feb 21	1.23	B	D4000
10:14:08.11	+00:37:36.6	LRIS	2015 Feb 21	1.239	A	Ca HK
10:14:00.32	+00:36:43.7	LRIS	2015 Feb 21	1.22	B	[O II] $\lambda$ 3727
10:14:08.13	+00:38:21.3	LRIS	2015 Dec 6	1.23	B	Ca HK, D4000
10:14:12.80	+00:38:12.2	MOSFIRE	2016 Feb 1	1.2318	A	H $\beta$ , [O III] $\lambda$ 4959, 5007
10:14:09.71	+00:41:11.1	LRIS	2016 Mar 6	1.226	B	[O II] $\lambda$ 3727
MOO J1521+0452 $z = 1.312$						
15:21:13.66	+04:53:28.0	LRIS	2016 Jul 5	1.308	B	Ca HK
15:21:12.10	+04:51:16.9	LRIS	2016 Jul 5	1.317	B	Ca HK
15:21:06.79	+04:52:09.1	LRIS	2016 Jul 5	1.312	B	Ca HK, D4000
15:21:04.90	+04:51:59.8	LRIS	2016 Jul 5	1.302	B	Ca HK, D4000
15:21:04.15	+04:52:12.4	LRIS	2016 Jul 5	1.32	B	Ca HK, D4000
15:20:59.35	+04:51:40.7	LRIS	2016 Jul 5	1.314	A	Ca HK, D4000
Foreground/Background Objects						
00:37:51.56	+33:10:07.0	LRIS	2016 Aug 5	1.453	A	[O II] $\lambda$ 3727, D4000
01:05:22.72	+13:23:55.2	LRIS	2015 Dec 4	0.229	A	[O II] $\lambda$ 3727
01:05:35.14	+13:23:36.9	LRIS	2015 Dec 4	0.248	A	[O II] $\lambda$ 3727, H $\alpha$ , H $\beta$
01:23:48.16	+25:46:01.2	LRIS	2017 Jul 20	0.2120	A	H $\alpha$ , H $\beta$
01:23:42.28	+25:46:31.4	LRIS	2017 Jul 20	0.4659	A	H $\alpha$ , [O III] $\lambda$ 4959, 5007
01:23:42.32	+25:47:17.5	LRIS	2017 Jul 20	0.4364	A	H $\alpha$
01:23:56.71	+25:46:31.7	LRIS	2017 Jul 20	1.4781	A	[O II] $\lambda$ 3727, Ca HK
10:14:11.57	+00:38:39.3	LRIS	2015 Feb 21	1.158	A	Ca HK, D4000
10:14:02.48	+00:34:53.0	LRIS	2015 Feb 21	0.326	A	H $\alpha$
10:14:13.36	+00:39:57.8	LRIS	2015 Dec 6	0.966	A	Ca HK, D4000, G
10:14:04.15	+00:41:03.5	LRIS	2015 Dec 6	0.981	A	[O II] $\lambda$ 3727, Ca HK, D4000
10:14:00.76	+00:40:23.2	LRIS	2015 Dec 6	0.3283	A	H $\alpha$ , [N II], Na D
15:21:08.78	+04:52:59.5	LRIS	2016 Jul 5	0.514	A	H $\alpha$ , [N II]
15:20:52.34	+04:51:32.0	LRIS	2016 Jul 5	0.489	A	H $\alpha$ , [N II]

**Note.**

<sup>a</sup> Qualities ‘‘A’’ and ‘‘B’’ denote redshifts of high and reasonable certainty, respectively (Stanford et al. 2014).

limit where our optical data are complete for all clusters, we characterize as stars objects falling above the line shown in Figure 6 that separates objects with the colors of stars from objects that are likely galaxies. Only objects bright enough to be clearly detected in even the shallowest of our optical images are so characterized to ensure a consistent cut across all clusters. We also match our catalogs to objects in the *Gaia*

DR2 catalog (Gaia Collaboration et al. 2016, 2018) with greater than  $3\sigma$  parallax, to confirm that objects known to be stars are the objects being rejected by this approach. We cannot do this for the SPT clusters due to a lack of comparable optical data.

Although the bulk of galaxies within  $r_{500}$  are cluster members, there is still a line-of-sight interloper contribution

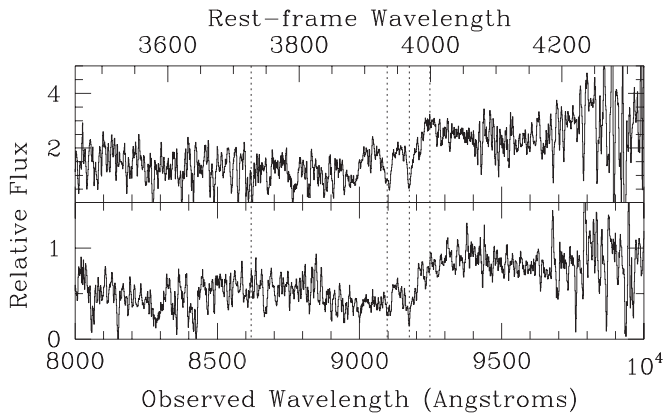


**Figure 3.** Spectra of two of the six confirmed members of MOO J1521+0452 at  $z = 1.31$ . The vertical lines show, left to right the locations of [O II]  $\lambda$  3727, Ca II K and H lines and the 4000 Å break.

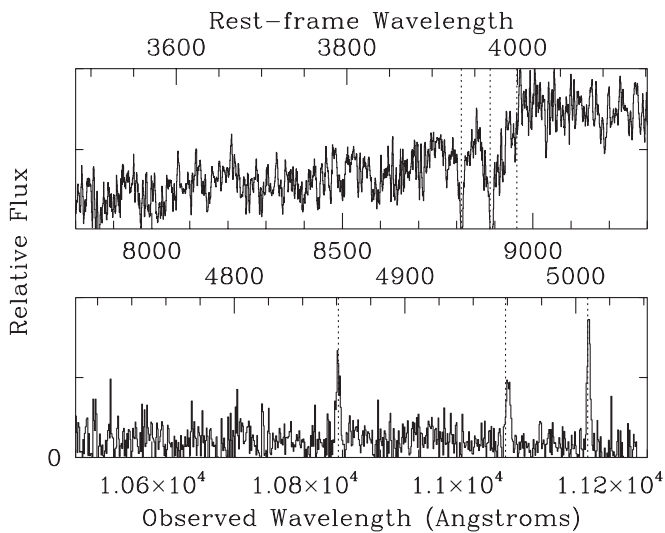


**Figure 4.** Spectra of confirmed MOO J1014+0038 cluster members from LRIS (top) and MOSFIRE (bottom), establishing a cluster redshift of  $z = 1.231$ . Left to right, the vertical lines of the top spectrum show the Ca II K and H lines and the 4000 Å break and the vertical lines of the lower plot show the H $\beta$  and [O III] emission features.

that must be subtracted. To account for this, we determine the expected contribution to the total flux density from field galaxies within the projected  $r_{500}$  area and subtract it off the flux density calculated from our cluster. We use the *Spitzer* Deep Wide-Field Survey (SDWFS; Ashby et al. 2009) to do this, applying the same brightness cuts to reject noncluster members as we apply to our cluster catalogs. For the clusters with optical data allowing the rejection of stars, we use optical photometry from the NOAO Deep Wide-Field Survey (NDWFS; Jannuzi & Dey 1999) to make the analogous stellar rejection in our background. For each cluster, we treat all remaining objects in the SDWFS catalog as though they were at the redshift of that cluster and calculate how much spurious luminosity they would add. We use the SDWFS field to determine our background because the IRAC imaging is deeper than that of our clusters and because SDWFS is large enough to smooth out small-scale variations in the background level. This background selection methodology does produce an appreciable systematic uncertainty in our results, as discussed in Section 5.4.

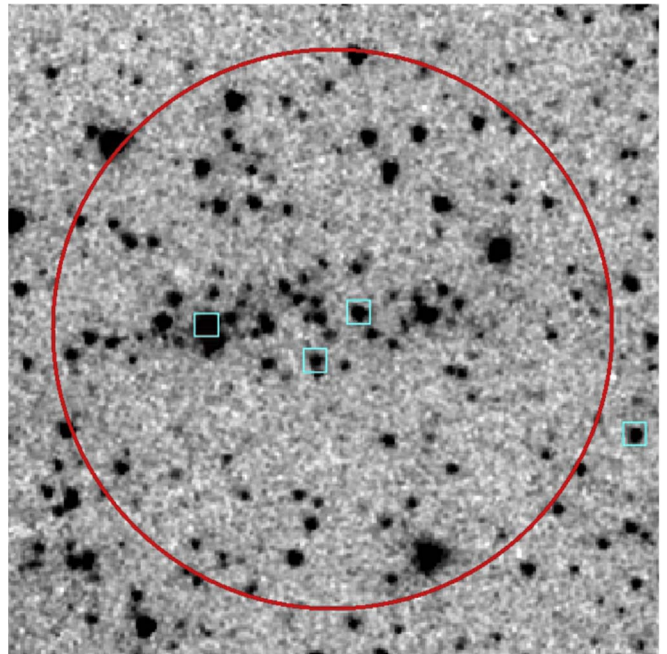


**Figure 5.** A  $170'' \times 170''$  *Spitzer*/IRAC  $3.6 \mu\text{m}$  image of MOO J1521+0452 showing an  $80''$  radius circle corresponding to the cluster  $r_{500}$  of 0.67 Mpc at  $z = 1.31$ . Only galaxies inside the red circle were included in the analysis. Cluster members with spectroscopic redshifts are marked with cyan squares.

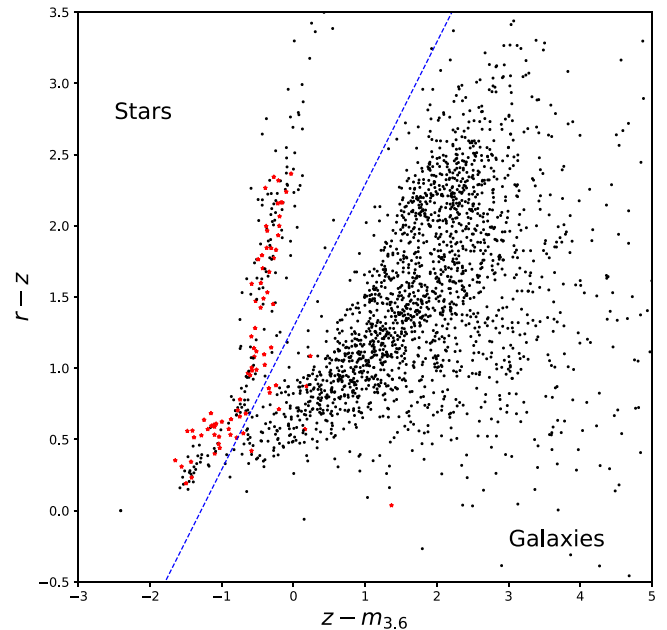


**Figure 6.** Combined color-color plot of all the MaDCoWS clusters for which there are GMOS data, showing  $r - z$  color plotted against  $z - m_{3.6}$ . Objects above the blue dashed line have colors consistent with being stars. Objects with  $\geq 3\sigma$  parallax in the *Gaia* DR2 catalog are plotted as red stars.

### 3.4. Completeness

To correct for incompleteness in our IRAC catalogs, we ran completeness simulations over the range of magnitudes at which we were looking using IRAF's *mkobjects* task in the *noao/artdata* package. For each cluster we added 10 random point sources in each half magnitude bin to the IRAC  $3.6 \mu\text{m}$  image, and ran SExtractor to see how many were recovered. We repeated this process 1000 times in each magnitude bin.

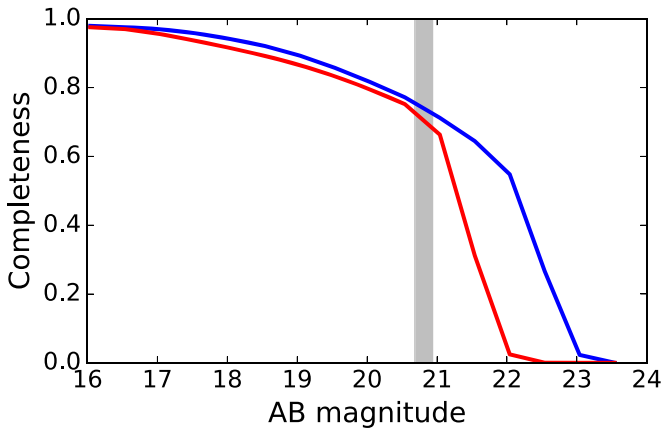


**Figure 7.** Average completeness curves for the MaDCoWS (red) and SPT (blue) IRAC  $3.6 \mu\text{m}$  images in AB magnitudes. The shaded region represents the range of maximum depths to which our analysis extends.

This was done for both the MaDCoWS and SPT clusters and we performed a similar analysis on the SDWFS  $3.6 \mu\text{m}$  image and on the optical images of the clusters. The average completeness curve for MaDCoWS and SPT are shown in Figure 7. At  $m^* + 1$ , the faint-end limit of our analysis, the catalogs of both surveys are approximately 70% complete, depending slightly on cluster redshift. Because our clusters have slightly different  $m^*$  (depending on redshift), our faint-end cutoff varies slightly, as shown in the figure.

## 4. Results

### 4.1. Stellar Mass

We calculate the stellar mass of the galaxies selected as possible cluster members using their rest-frame  $H$ -band luminosity. The rest-frame  $H$ -band is centered at the peak of the emission from the old, red stars that dominate the stellar mass of the galaxy. It is therefore a relatively low-scatter proxy for total stellar mass (e.g., Hainline et al. 2011) with a relatively small dependence on the overall spectral energy distribution (SED). At  $z \sim 1$  this is easily probed by the IRAC  $3.6 \mu\text{m}$  band. To determine the K-correction from observed IRAC  $3.6 \mu\text{m}$  to rest-frame  $H$ -band, we use EZGal (Mancone & Gonzalez 2012). We construct a synthetic galaxy SED with a Bruzual & Charlot (2003) 1 Gyr tau model, formation redshift  $z_f = 3$ , solar metallicity, and a Chabrier (2003) IMF. From this SED we derive a K-correction to the absolute magnitude in the  $H$ -band, from which we calculate  $L_H$ . We statistically correct our luminosities for incompleteness using the simulations described above. We use the same EZGal model to determine the stellar mass-to-light ( $M/L$ ) ratio in the  $H$ -band at the cluster redshift. This  $M/L$  ratio is different for each cluster, depending on the redshift, but is close to 0.34 on average. We apply the stellar  $M/L$  ratio to the sum of the luminosities of all the objects along the line of sight minus the background contribution estimated from SDWFS to get our final cluster stellar mass. Both the MaDCoWS and SPT clusters were analyzed in the same way and to the same depth to allow for direct comparison of the two samples.

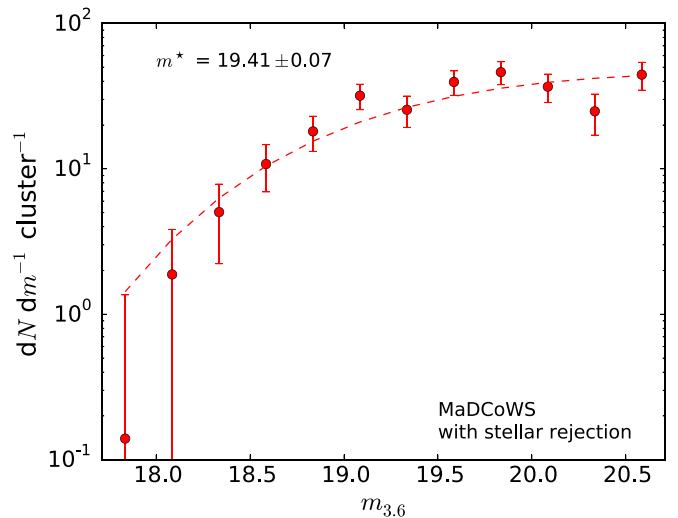


**Figure 8.** IRAC  $3.6 \mu\text{m}$  luminosity function for the five MaDCoWS clusters with optical data for stellar rejection. The solid circles are background-subtracted number per magnitude in each bin and the error bars are from Poisson noise. The dashed line is a best-fit Schechter function with a fixed  $\alpha = -0.8$  and the best-fit value of  $m^*$  is shown.

### 4.2. Estimating Stellar Corrections with Luminosity Functions (LFs)

Before calculating total stellar mass fractions, we need to account for foreground stars along the line of sight to our clusters. We do this by combining the optical stellar identification discussed in Section 3.3 with cluster LFs to estimate and correct the total impact from stars on our clusters that lack optical data.

The mean IRAC  $3.6 \mu\text{m}$  LF for the five MaDCoWS clusters with optical data for stellar rejection is shown in Figure 8. To make this LF we applied the membership cuts from Section 3.3, including stellar rejection from the optical data, to each cluster and evolution-corrected the members to  $z = 1$ . The galaxies from all the clusters were then binned in quarter-magnitude wide bins and the appropriate completeness and statistical background corrections were applied. The uncertainties on the values are Poisson errors.

We fit to the data a parameterized Schechter function of the form

$$\Phi(m) = 0.4 \ln(10) \Phi^* 10^{-0.4(m-m^*)(\alpha+1)} \exp(-10^{-0.4(m-m^*)})$$

(Schechter 1976) and we fix  $\alpha = -0.8$  as our data are not deep enough to constrain the faint-end slope. This choice is consistent with Mancone et al. (2010) and is a reasonable value for our data. The best-fit value is  $m^* = 19.41 \pm 0.07$  and we take this LF as representative of  $z = 1$  clusters independent of selection. The error on the  $m^*$  fit is calculated from the range of  $\chi^2$ , and is the same as the error calculated from bootstrap resampling. This value for  $m^*$  is somewhat brighter than, but close to that of Muzzin et al. (2008) who found  $m_{3,6}^* = 20.11 \pm 0.64$  (in AB magnitudes) for IRAC  $3.6 \mu\text{m}$  at  $z = 1.01$  and Mancone et al. (2010) who found  $m_{3,6}^* = 19.71 \pm 0.06$  at  $z = 0.97$ . It is also consistent with the value of  $m_{3,6}^* = 19.62^{+0.25}_{-0.20}$  found for infrared-selected clusters in a higher redshift bin ( $z = 1.45$ ) by Wylezalek et al. (2014).



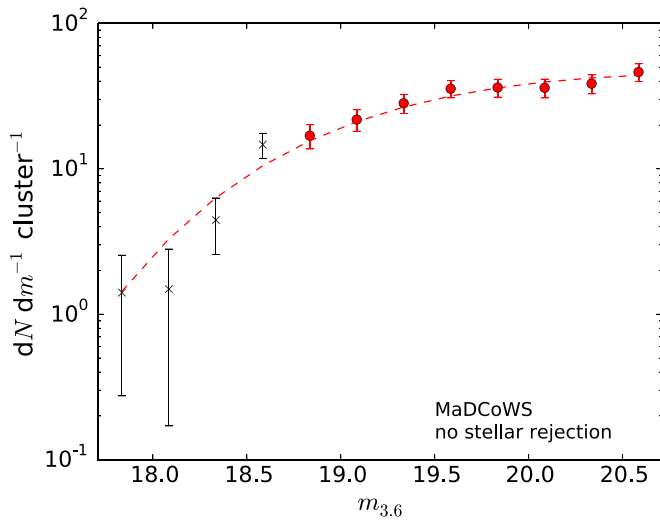


**Figure 9.** Mean IRAC  $3.6 \mu\text{m}$  luminosity function for the full sample of 12 MaDCoWS clusters with no optical rejection of stars. All of the points are background-subtracted number per magnitude in each bin and the error bars are from Poisson noise. The black crosses on the bright end are points with potential stellar contamination that we did not include when fitting the Schechter function, which is represented by the dashed red line. For the Schechter function, we fixed  $\alpha = -0.8$  and  $m^* = 19.41$  to match the luminosity function derived using optical stellar rejection.

We used a similar approach to make LFs for the full sample of 12 MaDCoWS clusters and for the SPT clusters, shown in Figures 9 and 10, respectively. The stellar contamination is more extensive for the SPT clusters because the sample extends to a lower galactic latitude, where there is more line-of-sight contamination, than does the MaDCoWS sample. We do not have adequate optical data for all of these clusters and thus do not attempt stellar corrections on a per-cluster basis. Rather, we construct a statistical stellar correction as follows. We fit the  $z = 1$  Schechter function determined above, allowing only  $\Phi^*$  to vary (i.e., with fixed  $\alpha = 0.8$  and  $m^* = 19.41$  as for the clusters without stellar contamination), to the points at the faint end of MaDCoWS and SPT LFs that show no evidence of stellar contamination (as determined by the SPT LF). These are the points plotted with filled circles in Figures 9 and 10; the unfit portion of the LFs, where there appears to be significant stellar contamination in the SPT LF, is plotted with black crosses. The ratios between the areas under these ‘no-stars’ fits for each sample, over the full magnitude range in this work, to the area under their respective observed LFs is the statistical stellar correction factor for that sample. We multiply the measured luminosity of each cluster by the correction factor of the sample to get the true luminosity for that cluster absent stellar contamination.

#### 4.3. Stellar Mass Fraction

To calculate  $f_*$ , we divide the stellar mass of the cluster by the total mass calculated from the SZ decrement described in Section 3.1. The stellar mass that we use is calculated by summing the completeness- and K-corrected  $H$ -band luminosity of every object projected within  $r_{500}$  of the cluster SZ centroid and subtracting the average background calculated from SDWFS. We then multiply this luminosity by the  $M/L$  ratio from our EZGal model for the cluster redshift and the average stellar correction for either the MaDCoWS or SPT

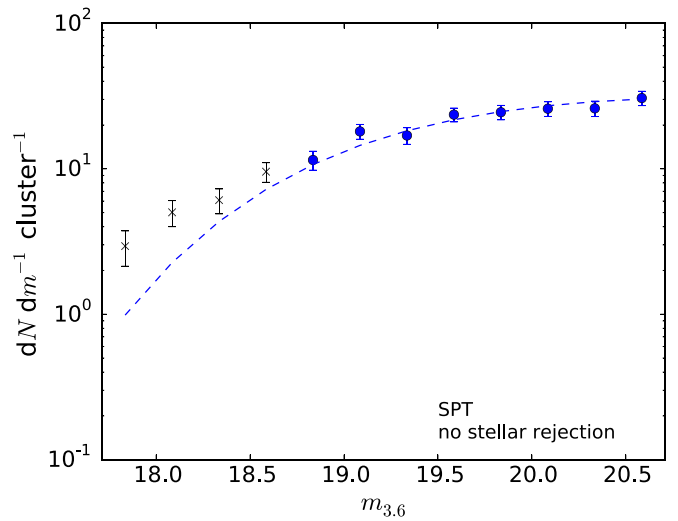


**Figure 10.** Mean IRAC  $3.6 \mu\text{m}$  luminosity function for the 33 comparison SPT clusters in this work. All of the points are background-subtracted number per magnitude in each bin and the error bars are from Poisson noise. The black crosses on the bright end are points with likely stellar contamination that we did not include when fitting the Schechter function, which is represented by the dashed blue line. For the Schechter function, we fixed  $\alpha = -0.8$  and  $m^* = 19.41$  to match the MaDCoWS LF. Note the stellar contamination at the bright end.

subsample calculated above. The systematic uncertainties inherent in this method are discussed in Section 5.4.

A plot of  $f_*$  versus  $M_{500}$  is shown in the upper panel of Figure 11, in which the red diamonds represent the infrared-selected MaDCoWS clusters and the blue circles represent the SZ-selected SPT clusters. The dashed green line is the low-redshift relation found by Gonzalez et al. (2013, hereafter G13) and the black error bars on either side of the plot indicate the systematic error introduced by the background subtraction. For each cluster in both samples the stellar mass fraction was calculated without any stellar rejection and then the average stellar correction for the appropriate sample, as calculated in Section 4.2, was applied in order to achieve a consistent stellar correction for all the clusters in each sample.

On average, the MaDCoWS clusters do not have significantly higher stellar mass fractions than the SPT clusters. There is a sizable systematic error, largely from the background subtraction, which is both larger than the statistical error and mass dependent, but it should affect both samples to the same degree and thus does not affect the direct comparison. This is discussed further in Section 5.4. To ensure that this comparison of  $f_*$  is unrelated to the trend of  $f_*$  with mass seen at low redshift, we also divide out the G13 trend line, as shown in the lower half of Figure 11. The errors on the resulting G13-normalized means for each sample are calculated from bootstrap resampling and shown as horizontal pink and cyan bars across the data. This normalization still does not show a significant difference between the mean of the 12 MaDCoWS clusters and the 33 SPT clusters, though there is still a relatively large error on the individual  $f_*$  values for both sets of clusters. Stellar masses and stellar mass fractions for the MaDCoWS clusters are given in Table 3.

As the vertical red and blue error bars in the lower panel of Figure 11 show, the scatter in the SPT stellar mass fractions is larger than that of the MaDCoWS clusters. There is also a much larger range in the SPT stellar mass fractions, with an order of magnitude separating the highest  $f_*$  clusters from the



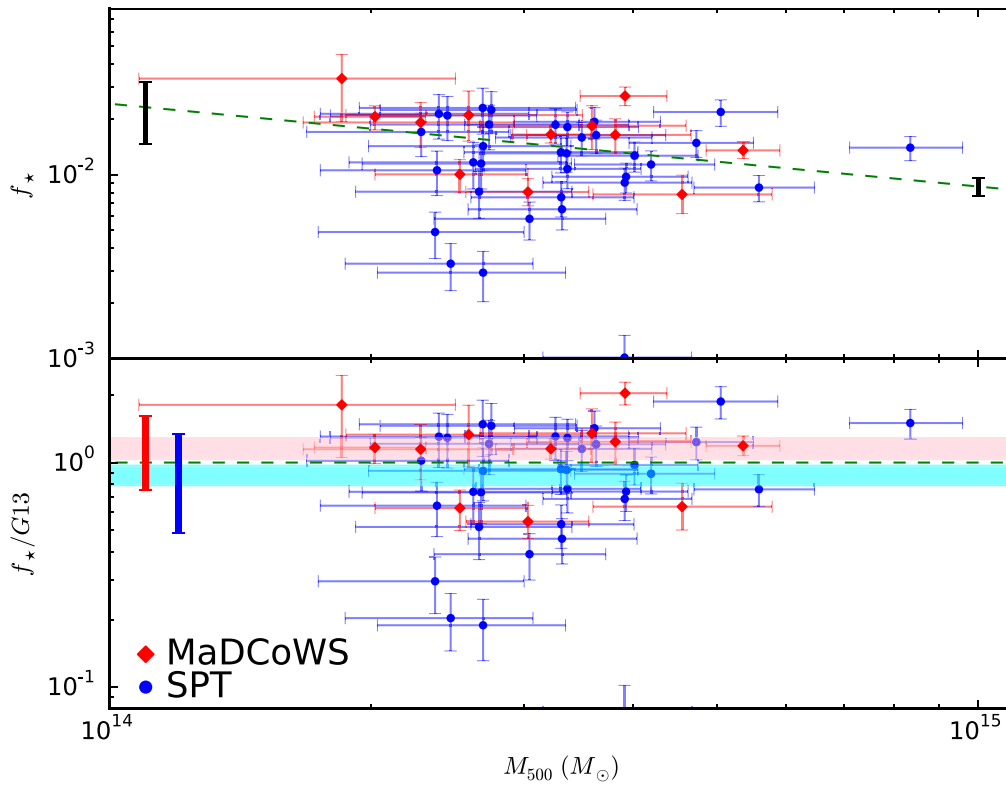


**Figure 11.** Top: stellar mass fraction vs. total mass for the MaDCoWS (red) and SPT (blue) clusters. The size of the systematic error in  $f_*$ , which varies with  $M_{500}$ , is represented by the black error bars on either end of the figure. The green dashed line is the low-redshift relation from G13. Bottom: the stellar mass fractions of each cluster normalized by the G13 relation vs. total mass. The error about the mean normalized  $f_*$  for both samples is calculated from bootstrap resampling and for MaDCoWS (SPT) is plotted in pink (cyan) across the figure. The scatter in normalized  $f_*$  is shown by the thick, vertical red (blue) error bars.

**Table 3**  
MaDCoWS Stellar Mass Fractions

ID	$z$	$M_{500}$ ( $10^{14} M_{\odot}$ )	$M_*$ ( $10^{12} M_{\odot}$ )	$f_*$ ( $10^{-2}$ )
MOO J0037+3306	1.139	$2.28^{+0.64}_{-0.61}$	$4.48 \pm 0.15$	$1.97^{+0.56}_{-0.53}$
MOO J0105+1323	1.143	$3.92^{+0.46}_{-0.44}$	$10.73 \pm 0.19$	$2.74^{+0.32}_{-0.31}$
MOO J0123+2545	1.229	$3.82^{+0.85}_{-0.80}$	$6.43 \pm 0.16$	$1.68^{+0.38}_{-0.35}$
MOO J0319-0025	1.194	$3.03^{+0.53}_{-0.46}$	$2.50 \pm 0.12$	$0.82^{+0.15}_{-0.13}$
MOO J1014+0038	1.230	$3.22^{+0.36}_{-0.31}$	$5.44 \pm 0.16$	$1.69^{+0.20}_{-0.17}$
MOO J1111+1503	1.32	$2.02^{+0.29}_{-0.30}$	$4.27 \pm 0.13$	$2.11^{+0.31}_{-0.32}$
MOO J1142+1527	1.189	$5.36^{+0.55}_{-0.50}$	$7.43 \pm 0.18$	$1.39^{+0.15}_{-0.13}$
MOO J1155+3901	1.009	$2.53^{+0.50}_{-0.51}$	$2.60 \pm 0.11$	$1.03^{+0.21}_{-0.21}$
MOO J1231+6533	0.99	$4.56^{+1.23}_{-0.96}$	$3.64 \pm 0.12$	$0.80^{+0.22}_{-0.17}$
MOO J1514+1346	1.059	$1.85^{+0.65}_{-0.77}$	$6.30 \pm 0.13$	$3.40^{+1.20}_{-1.42}$
MOO J1521+0452	1.312	$3.59^{+1.02}_{-0.92}$	$6.77 \pm 0.17$	$1.89^{+0.54}_{-0.49}$
MOO J2206+0906	0.951	$2.59^{+0.91}_{-0.72}$	$5.58 \pm 0.12$	$2.16^{+0.76}_{-0.60}$

lowest. The scatter in  $f_*$  seen in the MaDCoWS clusters is lower, but may not be representative of the general cluster population because of two selection biases. First, MaDCoWS is a stellar mass-selected cluster sample. As such, it may be biased toward systems with higher-than-average  $f_*$  values. Second, this particular subset of MaDCoWS clusters consists of the most significant detections from the first stage of the study, so may not be representative of the sample or of clusters as a whole. We do not expect the different redshift distributions to introduce a bias, however, as we find no evidence that  $f_*$  evolves with redshift. The SPT clusters, however, should provide a fair sample of the mean value and scatter of the stellar

mass fraction at the redshift of those SZ-selected clusters because they are selected independently of those components. We compared the stellar mass fractions of the MaDCoWS and SPT samples using a Kolmogorov–Smirnov test and found they were consistent with being drawn from the same underlying distribution.

The MaDCoWS sample contains three clusters known to be merging from high-resolution *Chandra X-ray Observatory* follow-up observations (Gonzalez et al. 2018). Previous studies of the effect merging has on the inferred  $Y_{SZ}$  mass of a cluster have produced mixed conclusions, with some (e.g., Poole et al. 2007; Krause et al. 2012) finding that major mergers bias the inferred  $Y_{SZ}$  mass of a system low for most of the observed timescale and others, (e.g., Marrone et al. 2012) finding the  $Y_{SZ}$  mass of merging clusters was overestimated. We do not expect merging to affect the observed richness of a cluster in the same way as the mass, however, so any effect on the inferred mass will bias our measurement of  $f_*$ . We do not have X-ray data for the full MaDCoWS sample or the comparison SPT sample, so we cannot fully remove mergers from our current analysis. However, the effect of excluding these clusters, for which we know our  $f_*$  measurement is likely to be wrong, is shown in Figure 12. The clusters are plotted in the same manner as the lower part of Figure 11; however, the three clusters known to be mergers are now plotted as open red diamonds and the mean is recalculated to exclude them. Although they are not large outliers, the three merging systems do have the highest normalized stellar mass fractions of the MaDCoWS sample. When they are excluded, the mean-normalized  $f_*$  for MaDCoWS decreases to  $f_*/G13 = 1.02 \pm 0.10$ , still higher than that of the SPT clusters, but now consistent within  $1\sigma$ . We also

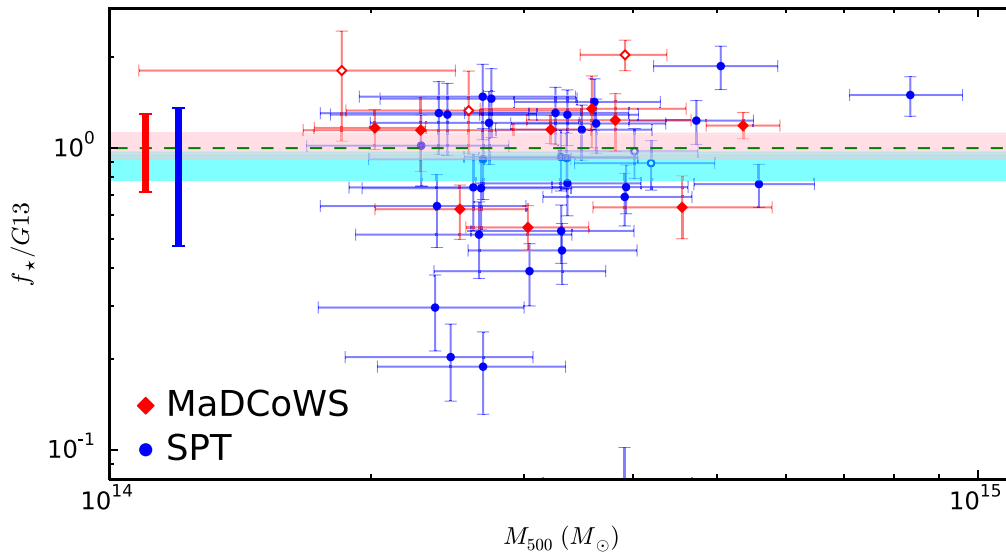


**Figure 12.** Same as the lower panel of Figure 11, with the merging MaDCoWS clusters (now shown as open diamonds) removed from the calculation of the mean normalized  $f_*$ . The effect of removing these clusters for which the total mass is known to be underestimated relative to the stellar mass is to drop the G13-normalized mean to  $f_*/G13 = 1.02 \pm 0.10$ ,  $1.0 \sigma$  higher than the unchanged SPT mean.

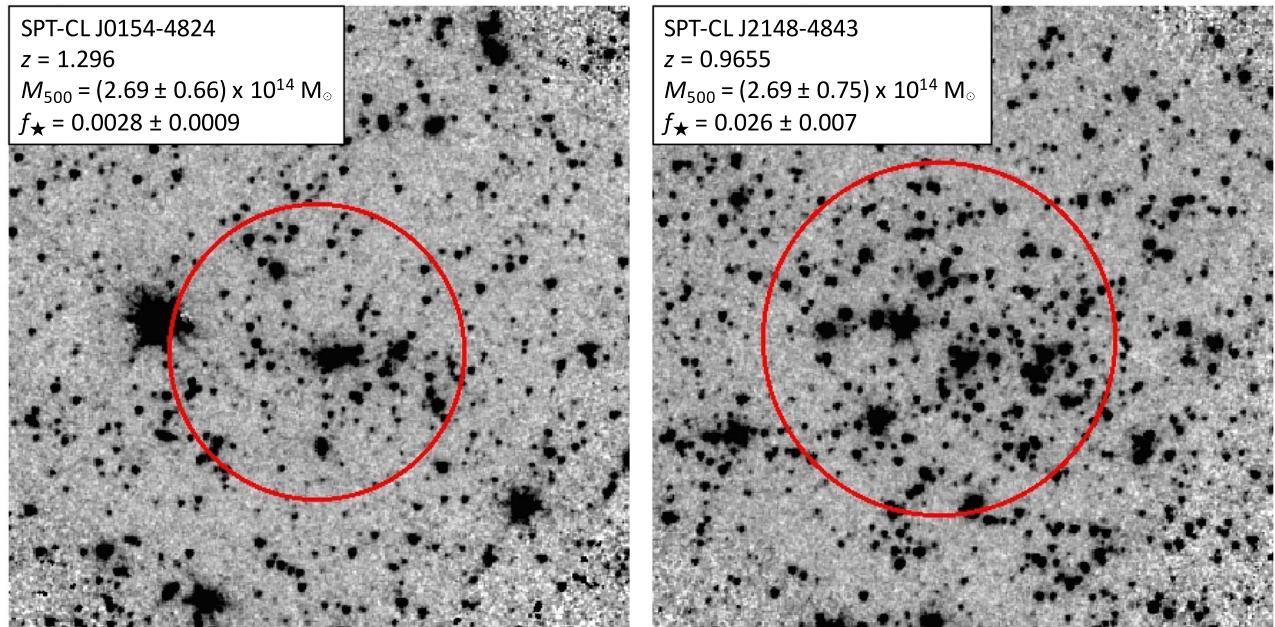


**Figure 13.** IRAC  $3.6 \mu\text{m}$  images of SPT-CL J0154-4824 (left) and SPT-CL J2148-4843 (right) showing the large difference in richness between clusters of the same halo mass. The projected  $r_{500}$  of each cluster is shown as a red circle. The difference in the angular size of the two circles is due to the redshift difference, which boosts the richness by 28% in the nearer cluster, but the comparison is relatively unaffected by the differential K-correction between the clusters as  $m^*$  in *Spitzer*  $3.6 \mu\text{m}$  is not significantly different between the two redshifts.

removed two clusters from the SPT sample identified as mergers in Nurgaliev et al. (2017, shown as open circles) which did not affect the mean  $f_*/G13$  of the SPT clusters.

## 5. Discussion

### 5.1. Comparison of Stellar Mass Fractions

As discussed above, Figures 11 and 12 show that the average stellar mass fraction in the MaDCoWS sample is not significantly higher than that of the SPT sample, though there is considerable scatter. To confirm that this is not an artifact of the trend of  $f_*$  with mass we normalized all the  $f_*$  measurements relative to the G13 relation and measured the

normalized mean  $f_*$  for both samples, shown in the lower panel of Figure 11. While the mean normalized  $f_*$  for MaDCoWS,  $f_*/G13 = 1.16 \pm 0.12$ , is higher than the corresponding mean for the SPT sample,  $f_*/G13 = 0.88 \pm 0.09$ , these are consistent within  $1.9\sigma$ .

### 5.2. Scatter in the Stellar Mass Fraction

The SZ-selected SPT clusters are best-suited to measure the scatter in  $f_*$  at high redshift as they are selected independently of stellar content and thus should represent an unbiased sampling of the stellar mass fraction in the full cluster population. The large range in  $f_*$  seen in this sample,

approximately an order of magnitude (see Figure 11), is perhaps surprising. As Figure 13 shows; however, this variation is clearly apparent in a visual inspection of the richnesses of two clusters with the same halo mass. Although both clusters in this figure have an SZ mass of  $M_{500} = 2.7 \times 10^{14} M_{\odot}$  (Bleem et al. 2015), SPT-CL J0154-4824 (left) has a stellar mass fraction of  $f_{\star} = (2.8 \pm 0.9) \times 10^{-3}$  whereas SPT-CL J2148-4843 (right) has a stellar mass fraction of  $f_{\star} = (2.6 \pm 0.7) \times 10^{-2}$ , an order of magnitude higher.

The MaDCoWS clusters in this work do not exhibit the same wide peak-to-trough range of stellar mass fractions nor as large a scatter, measured by the standard deviation of  $f_{\star}$ , presumably because they represent the high-richness end of an infrared-selected sample rather than a fair cross-section of all clusters. We attempt to quantify the *intrinsic* scatter in  $f_{\star}$  of both samples about their respective means, independent of our measurement errors, by assuming that the reduced chi-squared will be equal to unity when all the errors are included in the error budget. We therefore set the reduced chi-squared for each sample to unity and solve for the intrinsic scatter term. We find a significant intrinsic scatter,  $\sigma_{\ln f_{\star}} \sim 0.4$  dex for the SPT and  $\sigma_{\ln f_{\star}} \sim 0.3$  dex for MaDCoWS. This discrepancy supports the idea described in Section 4.3, that the MaDCoWS clusters may not provide a fair measurement of the scatter in  $f_{\star}$  due to their selection, but the SPT clusters should. By the same token, the MaDCoWS clusters should provide fair measurements of the scatter in  $f_{\text{gas}}$  that the SZ-selected surveys may not; this is a topic for future analyses with MaDCoWS. The SPT clusters show a larger intrinsic scatter in  $f_{\star}$  than is predicted in simulations, such as those of Kravtsov et al. (2005), Ettori et al. (2006), and Planelles et al. (2013). Very recently, IllustrisTNG (Pillepich et al. 2017) directly measured the scatter in the stellar-total mass relationship in simulated clusters at  $z = 0$  and  $z \sim 1$  and found a very low scatter in the relationship, only 0.07 dex. Some of the low values and high scatter in the SPT  $f_{\star}$  measurements may be due to the masses of low signal-to-noise clusters being overestimated. The clusters we use go to the low signal-to-noise limit of the SPT–SZ catalog and it is possible that some of these are lower mass clusters that scattered up above the cutoff. If we exclude these clusters, the intrinsic scatter of the SPT sample becomes consistent with that of the MaDCoWS clusters. This effect notwithstanding, understanding the baryonic processes causing the remaining large intrinsic scatter in stellar mass fraction, for which the MaDCoWS measurement of  $\sigma_{\ln f_{\star}} \sim 0.3$  dex may be considered a lower limit, is a challenge for the next generation of cosmological simulations.

### 5.3. Comparison to Other Works

Given the systematic uncertainties described above, it is difficult to make direct comparisons to other works with different systematics. Nevertheless, other works with similar methodologies provide good external checks on our results, and in particular allow us to test the effect of infrared- versus ICM-selection.

Chiu et al. (2018) also measured  $f_{\star}$  for 84 clusters from the SPT–SZ survey, some of which overlap with our SPT comparison clusters. We do not expect to find the same  $f_{\star}$  values for these clusters, as they use a slightly different cluster mass estimation (from de Haan et al. 2016) and an SED-fitting method to calculate stellar mass. Nevertheless, their average

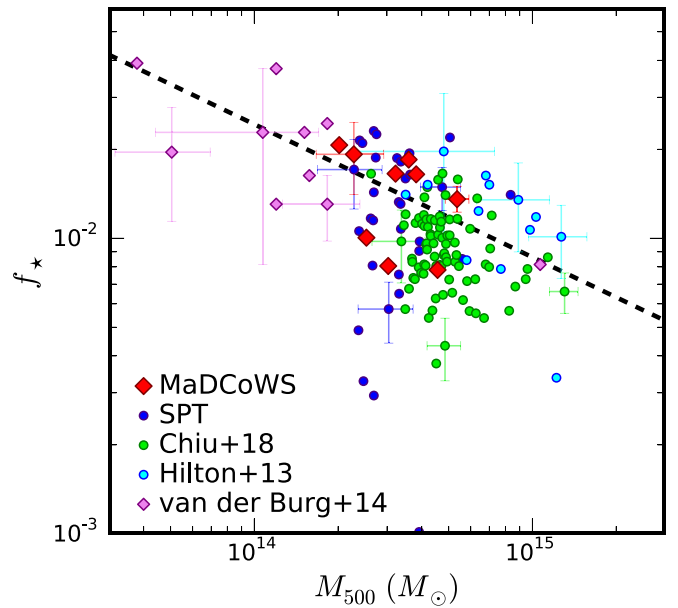


**Figure 14.** Comparison of the  $f_{\star}$  measured in this work (red diamonds, blue circles) to  $f_{\star}$  measured by Chiu et al. (2016; green circles), Hilton et al. (2013; cyan circles), and Burg et al. (2014; violet diamonds). All samples have been adjusted to be consistent with our methodology. Error bars are plotted for representative clusters for each sample.

value for  $f_{\star}$  is consistent with ours for the clusters in the same range of mass and redshift.

Hilton et al. (2013) reported stellar and total masses for a sample of 14 SZ-selected clusters from the Atacama Cosmology Telescope (ACT) in a redshift range of  $0.28 \leq z \leq 1.06$ . They have a mean stellar mass fraction of  $f_{\star} = 0.023 \pm 0.003$ , which is larger than what we find for our SZ-selected clusters. However, we use a Chabrier (2003) IMF to calculate stellar  $M/L$ , which results in lower stellar masses than the Salpeter (1955) IMF Hilton et al. (2013) used. Accounting for the difference in stellar mass resulting from the choice of IMFs (0.24 dex), our results are consistent with theirs.

Similarly, van der Burg et al. (2014) reported stellar and halo masses for 10 red sequence-selected clusters in a similar redshift range as ours. Using SED-fitting to determine the stellar mass of each galaxy, they find a mean stellar mass fraction for their IR-selected clusters of  $f_{\star} = 0.013 \pm 0.002$ . This is consistent with our MaDCoWS mean of  $f_{\star} = 0.015 \pm 0.005$ ; however, their method of calculating stellar mass has different systematics to ours. Correcting for these, as described below, shifts their average stellar mass fraction higher than the MaDCoWS value, but it remains consistent with the G13 trend due to their lower mass range. When we divide out the G13 line in the same manner as in Figure 11, we find they have an average normalized stellar mass fraction of  $f_{\star}/\text{G13} = 0.98$ , consistent with what we find for MaDCoWS.

Figure 14 shows  $f_{\star}$  versus  $M_{500}$  for our MaDCoWS and SPT clusters plotted alongside the values found by the studies described above. To make a meaningful comparison, we corrected the Hilton et al. (2013) and van der Burg et al. (2014) results to a Chabrier IMF. We further corrected the latter for the offset between SED-fitted and  $M/L$ -based stellar masses reported in that work. The infrared-selected MaDCoWS and van der Burg et al. (2014) clusters are plotted as red and violet diamonds, and the SZ-selected SPT clusters in this work, the



Chiu et al. (2018) SPT clusters and the Hilton et al. (2013) ACT clusters are plotted as blue, green, and cyan circles, respectively. The SZ-selected studies again find broadly similar stellar mass fractions to the infrared-selected studies, consistent with what we find here. The G13 relation is plotted as a dashed line and for each sample error bars are plotted for three representative clusters.

#### 5.4. Systematics

There are three main sources of systematic error in our analysis. The largest is due to our background subtraction; this error is represented by the black error bars in Figure 11. We quantify the size of this uncertainty by measuring the background luminosity from the SDWFS field in 1' radius cutouts across the field and measure the scatter in this background to estimate small-scale variation due to clustering. We add this scatter in quadrature with the field-to-field scatter derived by comparing SDWFS to similar measurements in the EGS (Davis et al. 2007) and COSMOS fields (Scoville et al. 2007). Since this is an error in the luminosity—and therefore the stellar mass—of each cluster, the size of the systematic error in  $f_*$  decreases with increasing  $M_{500}$ . This systematic error is a uniform shift affecting both the MaDCoWS and SPT clusters equally, so it does not affect our comparison of the infrared and ICM selection methods.

The second source of systematic uncertainty in the absolute value of  $f_*$  for our clusters is our choice of stellar  $M/L$ . There are two components to this systematic. The first is the choice of tau model described in Section 4.1, but this is a small effect. The 1.6  $\mu\text{m}$  bump is largely insensitive to the star formation history of the galaxy, so varying tau does not have a large effect on the  $M/L$  ratio. The second component is the choice of IMF. We use a Chabrier (2003) IMF, but other choices, such as the Salpeter (1955) IMF, are also common. This has a large effect on our  $M/L$  ratio, almost doubling it for a 1 Gyr tau model. However, because this is easily corrected for and does not affect any comparisons we make, we do not include it in our systematic error bar in Figure 11.

A final possible source of systematic uncertainty stems from our rejection of cluster nonmembers using magnitude cuts. Our choice of  $m^* - 2$  as a brightness threshold strikes a balance between maximizing the bright members included and minimizing the inclusion of bright foreground interlopers. Although this choice is a somewhat arbitrary threshold, changing it has only a small effect on our values for  $f_*$  because we already statistically correct for nonmember contamination, and one that is quite consistent from cluster-to-cluster. It does not make an appreciable difference to our analysis.

Our faint-end cutoff leads to a modest underestimate of the total stellar mass. Integrating an LF with  $\alpha = -0.8$  beyond  $m^* + 1$  suggests we could be missing  $\sim 25\%$  of the stellar mass from fainter galaxies. If we correct our stellar masses for this, the result is a simple multiplicative increase of all our  $f_*$  values, but by an amount less than both the scatter and the existing systematic error. Since this offset affects all clusters equally, it does not affect the scatter in either sample, or our comparison between the MaDCoWS and SPT stellar mass fractions. As a practical matter, the large uncertainties in  $\alpha$  and  $m^*$  make it difficult to accurately quantify the size of this uncertainty, and thus we choose not to include it in our analysis.

## 6. Conclusions

We have measured the stellar mass fractions of 12 infrared-selected clusters from MaDCoWS and 33 SZ-selected clusters from the SPT–SZ survey and found little difference in average  $f_*$  between the two selection methods. We measured  $f_*$  using IRAC 3.6  $\mu\text{m}$  images of the clusters at  $z \sim 1$  as a proxy for stellar mass along with total masses derived from SZ measurements. We found that when accounting normalizing over the trend of stellar mass fraction with total mass from G13, the infrared-selected MaDCoWS clusters have an average stellar mass fraction of  $f_*/G13 = 1.16 \pm 0.12$ , and  $f_*/G13 = 1.02 \pm 0.10$  after excluding three merging clusters. Both are higher than the average stellar mass fraction of  $f_*/G13 = 0.88 \pm 0.09$  for the SPT, but not significantly so.

We also compare our results to those of Hilton et al. (2013), van der Burg et al. (2014), and Chiu et al. (2016) who also looked at stellar mass fractions in cluster samples of comparable mass and redshift to ours. When we correct for the differences between our methodologies and those of the other studies, we find our results are consistent with all three and they support our result that infrared-selected clusters do not have an appreciably higher mean  $f_*$  than SZ-selected clusters. We also compare the value we calculate for  $m^*$  of the IRAC 3.6  $\mu\text{m}$  LF to that found by Muzzin et al. (2008), Mancone et al. (2010) and Wylezalek et al. (2014) and find similar results.

We found a larger range in the stellar mass fractions of individual clusters in the SPT sample than in our MaDCoWS clusters. It is possible that the SZ-selected SPT clusters give a fairer sample of the full range of  $f_*$  than the infrared-selected MaDCoWS clusters do. Future work with MaDCoWS will compare  $f_{\text{gas}}$  measurements in infrared- and SZ-selected cluster samples to look for a comparable selection effect in the latter.












Finally, we have presented SZ observations of seven new MaDCoWS clusters and new spectroscopic redshifts for five clusters. Among the SZ observations of the seven new MaDCoWS clusters is MOO J1521+0452, which at  $z = 1.31$  is one of the most massive clusters yet found at  $z \geq 1.3$ . Along with the previous discovery of a cluster of  $M_{500} = (5.36^{+0.55}_{-0.50}) \times 10^{14} M_{\odot}$  at  $z = 1.19$ , reported in Gonzalez et al. (2015), this further demonstrates the ability of MaDCoWS' nearly all-sky infrared selection to find the most massive clusters at high redshifts.

Support for CARMA construction was derived from the Gordon and Betty Moore Foundation, the Kenneth T. and Eileen L. Norris Foundation, the James S. McDonnell Foundation, the Associates of the California Institute of Technology, the University of Chicago, the states of California, Illinois, and Maryland, and the National Science Foundation. CARMA development and operations are supported by the National Science Foundation under a cooperative agreement, and by the CARMA partner universities; the work at Chicago was supported by NSF grant AST-1140019. Additional support was provided by PHY- 0114422. This work is based in part on observations made with the *Spitzer Space Telescope*, which is operated by the Jet Propulsion Laboratory, California Institute of Technology under a contract with NASA. Support for this work was provided by NASA through an award issued by JPL/Caltech. This publication makes use of data products from the *Wide-field Infrared Survey Explorer*, which is a joint project of the University of California, Los Angeles, and the Jet



Propulsion Laboratory/California Institute of Technology, funded by the National Aeronautics and Space Administration. Some of the data presented herein were obtained at the W.M. Keck Observatory, which is operated as a scientific partnership among the California Institute of Technology, the University of California and the National Aeronautics and Space Administration. The Observatory was made possible by the generous financial support of the W.M. Keck Foundation. This work was based in part on observations obtained at the Gemini Observatory, which is operated by the Association of Universities for Research in Astronomy, Inc., under a cooperative agreement with the NSF on behalf of the Gemini partnership: the National Science Foundation (United States), the National Research Council (Canada), CONICYT (Chile), Ministerio de Ciencia, Tecnología e Innovación Productiva (Argentina), and Ministério da Ciência, Tecnologia e Inovação (Brazil). This work has made use of data from the European Space Agency (ESA) mission *Gaia* (<https://www.cosmos.esa.int/gaia>), processed by the *Gaia* Data Processing and Analysis Consortium (DPAC, <https://www.cosmos.esa.int/web/gaia/dpac/consortium>). Funding for the DPAC has been provided by national institutions, in particular, the institutions participating in the *Gaia* Multilateral Agreement. Funding for this program is provided by NASA through the NASA Astrophysical Data Analysis Program, award NNX12AE15GB. Support for this work was provided by the National Aeronautics and Space Administration through *Chandra* Award Number GO6-17130X issued by the *Chandra* X-ray Center, which is operated by the Smithsonian Astrophysical Observatory for and on behalf of the National Aeronautics Space Administration under contract NAS8-03060.

### ORCID iDs

Mark Brodwin  <https://orcid.org/0000-0002-4208-798X>  
 Zubair Abdulla  <https://orcid.org/0000-0002-0664-7812>  
 Anthony H. Gonzalez  <https://orcid.org/0000-0002-0933-8601>  
 Daniel P. Marrone  <https://orcid.org/0000-0002-2367-1080>  
 Dominika Wylezalek  <https://orcid.org/0000-0003-2212-6045>  
 Wenli Mo  <https://orcid.org/0000-0002-9179-9801>  
 Emily Moravec  <https://orcid.org/0000-0001-9793-5416>  
 Daniel Stern  <https://orcid.org/0000-0003-2686-9241>  
 Matthew L. N. Ashby  <https://orcid.org/0000-0002-3993-0745>  
 Kyle Boone  <https://orcid.org/0000-0002-5828-6211>  
 Brian Hayden  <https://orcid.org/0000-0001-9200-8699>

### References

- Allen, S. W., Evrard, A. E., & Mantz, A. B. 2011, *ARA&A*, 49, 409  
 Andersson, K., Benson, B. A., Ade, P. A. R., et al. 2011, *ApJ*, 738, 48  
 Andreon, S. 2010, *MNRAS*, 407, 263  
 Arnaud, M., Pratt, G. W., Piffaretti, R., et al. 2010, *A&A*, 517, A92  
 Ashby, M. L. N., Stern, D., Brodwin, M., et al. 2009, *ApJ*, 701, 428  
 Bertin, E., & Arnouts, S. 1996, *A&As*, 117, 393  
 Bleem, L. E., Stalder, B., de Haan, T., et al. 2015, *ApJS*, 216, 27  
 Brodwin, M., Greer, C. H., Leitch, E. M., et al. 2015, *ApJ*, 806, 26  
 Brodwin, M., Stanford, S. A., Gonzalez, A. H., et al. 2013, *ApJ*, 779, 138  
 Bruzual, G., & Charlot, S. 2003, *MNRAS*, 344, 1000  
 Chabrier, G. 2003, *PASP*, 115, 763  
 Chambers, K. C., Magnier, E. A., Metcalfe, N., et al. 2016, arXiv:1612.05560  
 Chiu, I., Mohr, J., McDonald, M., et al. 2016, *MNRAS*, 455, 258  
 Chiu, I., Mohr, J. J., McDonald, M., et al. 2018, *MNRAS*, 478, 3072  
 Conroy, C., Wechsler, R. H., & Kravtsov, A. V. 2007, *ApJ*, 668, 826  
 Cutri, R. M. 2013, *yCat*, 2328, 0  
 Davis, M., Guhathakurta, P., Konidaris, N. P., et al. 2007, *ApJL*, 660, L1  
 de Haan, T., Benson, B. A., Bleem, L. E., et al. 2016, *ApJ*, 832, 95  
 Eisenhardt, P. R., Stern, D., Brodwin, M., et al. 2004, *ApJS*, 154, 48  
 Ettori, S., Dolag, K., Borgani, S., & Murante, G. 2006, *MNRAS*, 365, 1021  
 Fazio, G. G., Hora, J. L., Allen, L. E., et al. 2004, *ApJS*, 154, 10  
 Gaia Collaboration, Brown, A. G. A., Vallenari, A., et al. 2018, *A&A*, 616, A1  
 Gaia Collaboration, Prusti, T., de Bruijne, J. H. J., et al. 2016, *A&A*, 595, A1  
 Gettings, D. P., Gonzalez, A. H., Stanford, S. A., et al. 2012, *ApJL*, 759, L23  
 Giodini, S., Pierini, D., Finoguenov, A., et al. 2009, *ApJ*, 703, 982  
 Gonzalez, A. H., Decker, B., Brodwin, M., et al. 2015, *ApJL*, 812, L40  
 Gonzalez, A. H., Gettings, D. P., Brodwin, M., et al. 2018, arXiv:1809.06820  
 Gonzalez, A. H., Sivanandam, S., Zabludoff, A. I., & Zaritsky, D. 2013, *ApJ*, 778, 14  
 Gonzalez, A. H., Zaritsky, D., & Zabludoff, A. I. 2007, *ApJ*, 666, 147  
 Hainline, L. J., Blain, A. W., Smail, I., et al. 2011, *ApJ*, 740, 96  
 He, P., Feng, L.-L., & Fang, L.-Z. 2005, *ApJ*, 623, 601  
 Hilton, M., Hasselfield, M., Sifón, C., et al. 2013, *MNRAS*, 435, 3469  
 Högbom, J. A. 1974, *A&As*, 15, 417  
 Hook, I. M., Jørgensen, I., Allington-Smith, J. R., et al. 2004, *PASP*, 116, 425  
 Jannuzi, B. T., & Dey, A. 1999, in ASP Conf. Ser. 191, Photometric Redshifts and the Detection of High Redshift Galaxies, ed. R. Weymann et al. (San Francisco, CA: ASP), 111  
 Krause, E., Pierpaoli, E., Dolag, K., & Borgani, S. 2012, *MNRAS*, 419, 1766  
 Kravtsov, A. V., & Borgani, S. 2012, *ARA&A*, 50, 353  
 Kravtsov, A. V., Nagai, D., & Vikhlinin, A. A. 2005, *ApJ*, 625, 588  
 Lacy, M., Wilson, G., Masci, F., et al. 2005, *ApJS*, 161, 41  
 Lin, Y.-T., Mohr, J. J., & Stanford, S. A. 2003, *ApJ*, 591, 749  
 Lin, Y.-T., Stanford, S. A., Eisenhardt, P. R. M., et al. 2012, *ApJL*, 745, L3  
 Mancone, C. L., & Gonzalez, A. H. 2012, *PASP*, 124, 606  
 Mancone, C. L., Gonzalez, A. H., Brodwin, M., et al. 2010, *ApJ*, 720, 284  
 Marrone, D. P., Smith, G. P., Okabe, N., et al. 2012, *ApJ*, 754, 119  
 McLean, I. S., et al. 2010, Proc. SPIE, 7735, 77351E  
 McLean, I. S., et al. 2012, Proc. SPIE, 8446, 84460J  
 Mo, W., Gonzalez, A., Stern, D., et al. 2018, arXiv:1811.01826  
 Muzzin, A., Wilson, G., Lacy, M., Yee, H. K. C., & Stanford, S. A. 2008, *ApJ*, 686, 966  
 Nurgaliev, D., McDonald, M., Benson, B. A., et al. 2017, *ApJ*, 841, 5  
 Oke, J. B., Cohen, J. G., Carr, M., et al. 1995, *PASP*, 107, 375  
 Pillepich, A., Nelson, D., Hernquist, L., et al. 2017, arXiv:1707.03406  
 Planelles, S., Borgani, S., Dolag, K., et al. 2013, *MNRAS*, 431, 1487  
 Poole, G. B., Babul, A., McCarthy, I. G., et al. 2007, *MNRAS*, 380, 437  
 Rudy, D. J., Muhleman, D. O., Berge, G. L., Jakosky, B. M., & Christensen, P. R. 1987, *Icar*, 71, 159  
 Salpeter, E. E. 1955, *ApJ*, 121, 161  
 Schechter, P. 1976, *ApJ*, 203, 297  
 Scoville, N., Aussel, H., Brusa, M., et al. 2007, *ApJS*, 172, 1  
 Stanford, S. A., Gonzalez, A. H., Brodwin, M., et al. 2014, *ApJS*, 213, 25  
 Sunyaev, R. A., & Zeldovich, Y. B. 1970, CoASP, 2, 66  
 Sunyaev, R. A., & Zeldovich, Y. B. 1972, CoASP, 4, 173  
 van der Burg, R. F. J., Muzzin, A., Hoekstra, H., et al. 2014, *A&A*, 561, A79  
 White, S. D. M., Navarro, J. F., Evrard, A. E., & Frenk, C. S. 1993, *Natur*, 366, 429  
 Wright, E. L., Eisenhardt, P. R. M., Mainzer, A. K., et al. 2010, *AJ*, 140, 1868  
 Wylezalek, D., Vernet, J., De Breuck, C., et al. 2014, *ApJ*, 786, 17  
 Zhang, Y.-Y., Laganá, T. F., Pierini, D., et al. 2011, *A&A*, 535, A78